Continental Shelf Research 31 (2011) 1688–1700

Contents lists available at ScienceDirect

Continental Shelf Research

journal homepage: www.elsevier.com/locate/csr

Research papers

Parameterization of bedform morphology and defect density with fingerprint analysis techniques

Adam Skarke*, Arthur C. Trembanis

University of Delaware, College of Earth, Ocean, and Environment, Department of Geological Sciences, Newark, DE 19716, USA

ARTICLE INFO

Article history:
Received 27 January 2011
Received in revised form
15 July 2011
Accepted 21 July 2011
Available online 28 July 2011

Keywords:
Ripple
Fingerprint
Bedform
Morphodynamics
Sediment
Parameterization

ABSTRACT

A novel method for parameterizing the morphology of seafloor ripples with fingerprint analysis numerical techniques is presented. This fully automated analysis tool identifies rippled areas in two-dimensional imagery of the seafloor, and returns ripple orientation and wavelength as well as a new morphological parameter, the spatial density of ripple defects. In contrast to widely used manual and spectral parameterization methods, this new technique yields a unique probability distribution for each derived parameter, which describes its spatial variability across the sampled domain. Here we apply this new analysis technique to synthetic and field collected side-scan sonar seafloor images in order to assess the methods capacity to define bed geometry across a wide range of simulated and observed morphological conditions. The resulting orientation and wavelength values compare favorably with those of the existing manual and spectral parameterization methods, and are superior under environmental conditions characterized by low signal to noise ratios as well as high planform ripple sinuosity. Furthermore, the resulting ripple defect density values demonstrate correlation with ripple orientation, wave direction, and the Shields parameter, which is consistent with recent investigations that have theoretically linked this parameter to hydrodynamic forcing conditions. The presented fingerprint analysis method surpasses the capacity of existing methods for ripple parameterization and promises to yield greater insight into theoretical and applied problems associated with the temporal and spatial variability of ripple morphology across a wide spectrum of marine environments.

1. Introduction

Small-scale bedforms known as ripples are ubiquitous in nearshore coastal systems and occur at depths where shear stress generated by wave and current energy is sufficient to initiate transport of unconsolidated sediment. Over finite time periods, causality between wave and current induced hydrodynamic forcing at the bed and coincident ripple morphology is known to be bidirectional (Nielsen, 1981; Wright, 1995). A number of laboratory as well as field investigators have empirically established and analytically modeled this relationship for a variety of environments (see summaries by Wiberg and Harris, 1994; Doucette, 2002; and Soulsby and Whitehouse, 2005). These modeling efforts, especially field based ones, were initially limited by the observational challenges of accurately recording bed geometry and coincident hydrodynamic conditions over sustained time periods (Davies and Thorne, 2008). More recent developments in acoustic oceanographic instrumentation have substantially improved observational capacity resulting in ripple models with greater accuracy and sophistication (Davies and Villaret, 2002; Traykovski, 2007; Hay, 2008; Tang et al., 2009). Within the last decade, the development and commercial availability of acoustic Doppler current profiler and acoustic Doppler velocimeter technology has allowed for precise observation of water motion associated with the bottom boundary layer. The resulting acoustic backscatter data is processed with standardized physical theories of nearbed turbulence, which yield high-resolution time series observations of parameters, such as flow direction and speed, which quantitatively describe the hydrodynamic processes acting on the bed. Similar developments in acoustic backscatter instrumentation, specifically the side-scan sonar (Rubin et al., 1983; Hay and Wilson, 1994; Irish et al., 1999; Hay and Mudge, 2005), have allowed for precise observation of seafloor bedform morphology (Thorne and Hanes, 2002). However, in contrast to the hydrodynamic instrumentation, there is not yet a standardized method for processing side-scan acoustic backscatter data in order to yield parameters that describe the fundamental physical characteristics of bed morphology. Therefore, it is imperative to determine which parameters are most representative of ripple morphology, and the best way to extract those parameters from side-scan data, in order to accurately understand ripple evolution and validate modeling of ripple response to hydrodynamic forcing. Our objective here is to present an improved method for

* Corresponding author. Tel.: +1 302 981 9908; fax: +1 302 831 4158.
E-mail address: askarke@udel.edu (A. Skarke).

0278-4343/$ - see front matter © 2011 Elsevier Ltd. All rights reserved.
doi:10.1016/j.csr.2011.07.009

deriving established ripple morphology parameters (ripple wavelength and orientation), as well as to introduce a new parameter (ripple defect density), which is uniquely representative of rippled bed state.

Investigators have generally extracted three fundamental parameters from seafloor images in order to define bedform morphology: ripple height, wavelength, and the orientation of ripple crests. These three parameters are important, because a significant body of research indicates a relationship between them and the transport vector of flow (Nielsen, 1981; Grant and Madsen, 1982; Mogridge et al., 1994; Li et al., 1996; Wiberg and Harris, 1994). Investigations employing two-dimensional optical or acoustic imagery of the seafloor have generally considered only ripple wavelength and orientation as ripple height cannot be derived from planform observations without the use of specialized methods and apparatuses (Li and Amos, 1998; Traykovski et al., 1999; Tang et al., 2009).

Some investigations involving the comparison of hydrodynamic flow and bedform characteristics have relied on morphologic parameters derived from manual qualitative interpretation of seafloor images (Traykovski et al., 1999; Hay and Mudge, 2005). This methodology is subject to a number of sources of data uncertainty. First, manual measurements of bedform wavelength and orientation rely on individual perception and interpretation of a seafloor image, and because of this, observations can show significant variability between practitioners (Englert, 2010). Additionally, repeated processing of the same dataset multiple times by a single operator produces variability between measurements indicating that manual observations of seafloor morphology may not be reliably repeatable. Furthermore, this method requires the visual derivation of a single wavelength and orientation value for an entire spatial domain, thus reducing a complex surface to a single value in an unsystematic manner. A rippled surface can only be accurately defined with a single wavelength and orientation value if they are homogeneously two-dimensional and field observations suggest that such a bed state rarely, if ever, exists. Rather, bedform morphology often exhibits a distributed range of wavelengths and orientations across the observed domain. These parameters can best be described through a statistical treatment of a population of spatially distributed observations, rather than single representative value determined visually. However, when field data is considered it quickly becomes obvious that manual extraction of all wavelength and orientation data from an image of a ripple domain, in order to build a statistically significant population of observation for statistical analysis, is not a practical processing option.

To overcome the limitations of manual analysis, investigators have developed an automated method to extract ripple wavelength and orientation parameters from the power spectra of seafloor images transformed into the frequency domain. The most common approach is the transformation of ripple image data from a one- or two-dimensional spatial domain into the frequency domain, where orientation and wavelength data are derived from the relative positions of power spectral peaks (Voulgaris and Morin, 2008; Cheel and Hay, 2008; Maier and Hay, 2009). For one-dimensional analysis, the acoustic backscatter amplitude along a single azimuthal direction, typically orthogonal to the direction of expected ripple crest, is transformed to radial power spectra, with spectral peaks indicating ripple frequency and thus wavelength (Cheel and Hay, 2008). For two-dimensional analysis, a raster image of the bedform domain is preprocessed to an appropriate size and resolution. A two-dimensional frequency transform such as the Fourier (Voulgaris and Morin, 2008) or the Radon (Maier and Hay, 2009) is carried out on the data, resulting in the generation of a two-dimensional power spectrum projected in frequency space. The resultant plot exhibits a series of spectral peaks, which are symmetrical about the origin. The distance between the origin and spectral peak of greatest magnitude is representative of the ripple wavelength in the domain, while an azimuthal bearing from the origin to the same spectral peak is representative of the orientation of the ripple crest in the domain. For both one- and two-dimensional frequency transforms, the shape of the spectral peak represents the total variability in bed morphology across the domain, and the uncertainty of the observations, which may arise through instrumental error or natural processes such as the presence of suspended sediment in the water column. A very tall and narrow spectral peak would represent a bed with minimal variability (two-dimensional ripples) and/or lower uncertainty, while a shorter and wider spectral peak would represent a bed with high variability (sinuous ripples) and/or greater uncertainty.

The frequency-transform method for deriving wavelength and orientation parameters from ripples represents a significant improvement over the manual approach in a number of ways. First, it is automated, allowing for the processing of images in a more efficient and practical way than the manual method. Additionally it does not rely on human visual interpretation of images to assign parameters; therefore, it is free of individual observational bias and is standardized as well as repeatable. Finally, the frequency-transform method expresses bed morphology as frequency spectra, the shape of which represents uncertainty as well as variability across the spatial domain and can be quantified with statistical analysis. Although the frequency-transform method represents a significant improvement over the manual method it nonetheless has limitations. Chief among these is the fact that the morphological, environmental, and instrumental factors contributing to the power spectra shape are not independent, and cannot be deconvolved. The spectral shape is representative of the total morphological variability and uncertainty in the domain; however, the contribution of each cannot be independently extracted, thus there is no way to quantify the variability of individual parameters such as orientation and wavelength. Additionally, the frequency-transform method requires that a square image domain be sampled, which often necessitates the inclusion of imagery from non-rippled or obscured areas such as an acoustic shadow from instrumentation (Fig. 1B). This problem can be overcome through careful

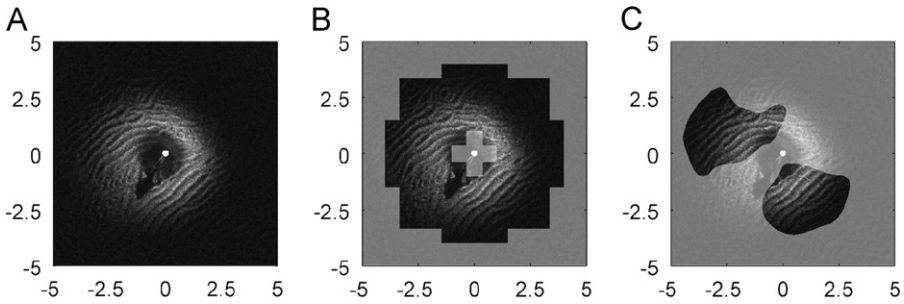

Fig. 1. (A) An example rotary sonar image (axes in meters). (B) The image sampling scheme used for the spectral method, with 8 individual sub-sampled squares (Voulgaris and Morin, 2008). (C) The image sampling scheme used for fingerprint analysis method based upon the filtering of non-rippled portions of the domain.

manual sub-sampling of an image; however, this process negates many of the advantages spectral methods have over manual method including automation and standardization. The prescribed inclusion of this data, which yield no information about ripples, leads to higher levels of spectral noise, which obscures the desired morphological signal and introduces a greater degree of uncertainty in the results.

Here we introduce a more sophisticated method for parameterization of rhythmic bedform morphology and demonstrate, through comparison of both synthetic and field results, its capacity to address the shortcomings of both the manual and the spectral approaches. This novel method utilizes image-processing routines developed within the biometrics research community for the parameterization and identification of fingerprints. The challenges associated with fingerprint analysis and ripple morphology parameterization are very similar. In both cases, the goal is to process a two-dimensional representation of a three-dimensional ridge and valley surface in order to isolate and catalog the fundamental defining morphological parameters. An existing numerical technique for fingerprint analysis was modified for application to rippled seafloor imagery. Modifications primarily address the subtle differences between seafloor and fingerprint images such as acoustic signal attenuation, and the fact that in a fingerprint image grayscale intensity is a function of surface elevation, while in a side-scan sonar image it is a function of surface slope relative to the acoustic transducer as well as distance from the transducer (sonar range). In contrast to existing approaches, the fingerprint analysis method assigns a localized orientation and wavelength value at each pixel of the domain, creating a unique population of spatially distributed observations for each parameter. These individual distributions can be addressed statistically in order to define a representative value for each parameter (mean or median) and to quantify the variability of that parameter across the sampled domain (standard deviation). Furthermore, because parameters are computed for a localized area around each pixel, the resulting values can be selectively filtered to remove data from areas that fail to meet predefined criteria for rippled morphology, such as flat seafloor or areas obscured by acoustic shadows from instrumentation or mooring equipment (Fig. 1C). This spatial filtering process significantly reduces the noise and uncertainty present in the extracted wavelength and orientation values. Finally, the fingerprint analysis technique introduces the ability to derive parameters in addition to orientation and wavelength from ripple imagery. Most promising is the capacity to determine the location, quantity, and relative position of minutiae structures (ripple terminations and bifurcations) otherwise known as "ripple defects" (Huntley et al., 2008). Investigators have theoretically related the density of ripple defects within a rippled seafloor domain to bedform migration rates (Werner and Kocurek, 1999), as well as the temporal evolution of ripple height and wavelength (Huntley et al., 2008). Others have noted high concentrations of defects in anorbital ripple fields reorienting after rapid changes in wave direction (Maier and Hay, 2009). Finally, Kocurek et al. (2010) suggest that defect creation and migration can play a significant role in regulating the rate and direction of bed evolution between initial and more developed states.

2. Methods

2.1. Data collection and instrumentation

Field observations of seafloor morphology and coincident hydrodynamic flow on (1) a prograding ebb-tidal shoal (Hen and Chickens Shoal, DE) and (2) a transgressive barrier shoreface (Cedar Island, VA) (Fig. 2) were recorded for durations of 23 and 40 days, respectively, through conditions that varied from fair weather to significant tropical and extratropical storm events. Both locations are characterized by medium grained unconsolidated sand ($d50 \cong 0.25$ mm), and

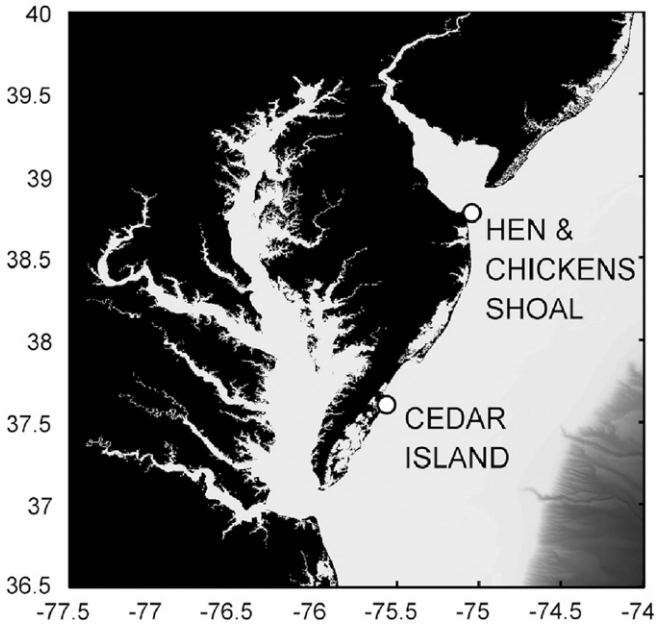

Fig. 2. Mid-Atlantic Bight. Locations of instrument deployments marked with white circles.

the instrument deployment depths were 7.4 m and 9.2 m, respectively. Hen and Chickens Shoal is located adjacent to the mouth of the Delaware Bay and is characterized by significant wave and tidal current energy, which generally alternate in dominance on a semi-diurnal time scale. Observed waves and flood/ebb currents both consistently produce bed shear stresses capable of transporting local sediment and reshaping the seafloor morphology. The relatively high frequency of alternation in the dominant energy source within the system results in an extremely dynamic bed that rarely attains morphologic equilibrium with any given hydrodynamic regime (i.e. never fully wave or current dominated). The Cedar Island transgressive barrier shore face is dominated by wave energy, which is consistently much greater than that of the current. Wave shear stress episodically exceeds the threshold required to mobilize sediment, so that the bed state alternates between being dynamically controlled and relict. Both locations consistently exhibit ripple morphology, which evolves in form and magnitude over time.

Field instrumentation consisted of a seafloor frame outfitted with a Nortek (Oslo, Norway) upward looking acoustic wave and current (AWAC) profiler, and an Imagenex (Port Coquitlam, Canada) tilt head rotary imaging side-scan sonar linked to an ASL (Sidney, Canada) IRIS power source and data logger system. The upward looking 1 MHz AWAC was deployed at 0.45 m above the bed and recorded Doppler current vector values from 0.5 m depth bins every 5 min for the duration of both deployments. The AWAC was equipped with acoustic surface tracking (AST) which directly measures the free surface elevation with an upward pointing single beam sonar during wave burst, which occur for 17 min once an hour. The resulting time series was analyzed to derive direct measurements of significant wave height and period, and then combined with near surface orbital velocity measurements to derive directional wave spectra. Current velocity values have an instrumental uncertainty of 1 cm/s, an accuracy of 1% of the measured value ± 0.5 cm/s. Wave height values have an instrumental uncertainty of 1 cm and an accuracy of 1% of the measured value. Wave direction values have an instrumental uncertainty of 0.1° and an accuracy of 2°. The Imagenex 2.25 MHz rotary imaging side-scan sonar was located on the same frame as the AWAC for both deployments. The acoustic aperture was positioned 1 m above the bed with a downward tilt of 17° from the vertical. The sonar

completed four 360° revolutions once an hour. Each revolution generating an acoustic backscatter image with a median resolution of 2.4 cm^2 and a seafloor coverage of 254 m^2. An ASL data logger running IRIS command and control software provided power, control, and data storage for the rotary sonar during both deployments.

Field observations of seafloor morphology across a sorted bedform feature were collected at a shallow ($H \cong 12$ m) inner-shelf sight (Martha's Vineyard Coastal Observatory, Massachusetts). The location is characterized by bimodal sediment grain size distribution, and the dominant morphological forcing mechanism is episodic wave events, which result in significant bed evolution (Mayer et al., 2007). A 0.25 km^2 mosaic acoustic image of the seafloor was collected with a Marine Sonic 900 Khz side-scan sonar mounted on a Gavia autonomous underwater vehicle operating 6 m above the bed. A detailed description of the data collection methods and instrumentation is presented by Trembanis et al. (2010).

2.2. Hydrodynamic data processing

Observed hydrodynamic conditions were processed and presented in order to qualitatively assess if ripple geometry and ripple defect occurrence as determined by the fingerprint analysis method correlate with wave direction, and the Shields parameter, as indicated by a numerous investigations (Wright, 1995; Soulsby and Whitehouse, 2005; Huntley et al., 2008; Werner and Kocurek, 1999; Maier and Hay, 2009; Kocurek et al., 2010). Hydrodynamic data collected with the AWAC profiler is imported with the instrument manufacturer's software and converted into time series of flow magnitude and direction in a geographical reference plane. The current induced forces acting on the bed are parameterized with the mean current Shields parameter:

$$\theta_c = \frac{\tau_c}{(\rho_s - \rho) g d} \tag{1}$$

where ρ_s and ρ are the density of the sediment and water, respectively, g is the gravitational acceleration, d is the sediment median grain size, and τ_c is the bed shear stress due to current, calculated using the quadratic stress law:

$$\tau_c = \rho C_D U^2 \tag{2}$$

where U is the depth averaged current velocity and C_D is the coefficient of drag given by

$$C_D = [0.40/1 + \ln(z_0/h)]^2 \tag{3}$$

And z_0 is expressed as $d/12$ for hydrodynamically rough flow (Soulsby, 1997).

Assuming a fully logarithmic profile. Linear wave theory is used to convert direct observations of significant wave height, period, and depth to significant bottom orbital velocity u_0 and diameter d_0:

$$u_0 = \frac{\pi H_s}{T \ \sin h(kh)} \tag{4}$$

$$d_0 = \frac{H_s}{\sin h(kh)} \tag{5}$$

The wave-induced forces acting on the bed are parameterized with the wave Shields parameter:

$$\theta_w = \frac{\tau_w}{(\rho_s - \rho) g d} \tag{6}$$

where τ_w is the maximum bottom shear stress given by

$$\tau_w = \frac{1}{2} \rho f_w {u_b}^2 \tag{7}$$

where f_w is the wave friction factor (Swart, 1974):

$$\begin{aligned} f_w &= 0.3 && \text{for } r \le 1.57 \\ f_w &= \exp[5.213 (k_s/a_s)^{0.194} - 5.977] && \text{for } r > 1.57 \end{aligned} \tag{8}$$

where

$$r = \frac{u_b T}{2 \pi k_s} \tag{9}$$

The Nikuradse equivalent sand grain roughness is defined as

$$k_s = 2.5 d \tag{10}$$

And the near bed wave orbital amplitude is given by

$$a_s = \frac{d_0}{2} \tag{11}$$

The resultant time series of hydrodynamic parameters and forcing derivatives are plotted in Fig. 3.

Note that the skin friction shear stress, based on grain roughness, was used to calculate the wave Shields parameter because reliable observations of ripple height as well as measurements of suspended sediment concentration, necessary to calculate form drag and movable bed roughness, respectively, were unavailable. Previous investigations have indicated that existing models of ripple geometry are not appropriate for the prediction of form drag, given non-equilibrium and combined forcing (waves and currents) hydrodynamic conditions at the study site (Skarke and Trembanis, 2008). Additionally, it is widely acknowledged that the skin friction component of shear stress is primarily responsible for sediment entrainment and transport (Nielsen, 1992; Wright, 1995; Soulsby, 1997; Traykovski et al., 1999). However, it is well understood that turbulent dissipation over rippled beds generates structured vortices, which directly influence the transport of suspended sediments (Grant and Madsen, 1982; Nielsen, 1992; Li et al., 1996; Soulsby, 1997). Accordingly, a more precise calculation of boundary layer flow, bed stress, and turbulence could be derived from the consideration of ripple height and future investigations would do well to include the necessary apparatuses and instruments to accurately observe these parameters (Li and Amos, 1998; Traykovski et al., 1999; Tang et al., 2009).

2.3. Morphological data processing

Acoustic backscatter imagery was analyzed with processing routines in Matlab computational software. All acoustic data is referenced in a polar coordinate system relative to the instrument as a bearing, range, and intensity. This data is first slant-range corrected to convert range to distance across the seafloor. Next, the bearing and range data is converted to Cartesian coordinates (x,y) with each point being associated with a scalar backscatter intensity value. Finally, these x, y, and backscatter values are converted to geographical coordinates for synthesis with coincident hydrodynamic data. Once the image domain is in geographical coordinates and raster format it is prepared for manual, spectral, and fingerprint analysis.

Manual analysis was conducted with a graphical user interface (GUI) code created with LabVIEW computational software. The software first imports a rotary sonar image and projects it in geographical coordinates within a GUI window. Next the program projects a series of equally spaced parallel dashed lines over the image. A user can then manipulate a knob in the GUI to adjust the orientation of the projected lines and a slider control to adjust the spacing of the lines to match as closely as possible the rhythmic pattern on the underling image. When the user is satisfied that they have matched the underlying images they then push a button in the GUI which saves the data from the projected lines as wavelength and orientation for that particular sonar image and

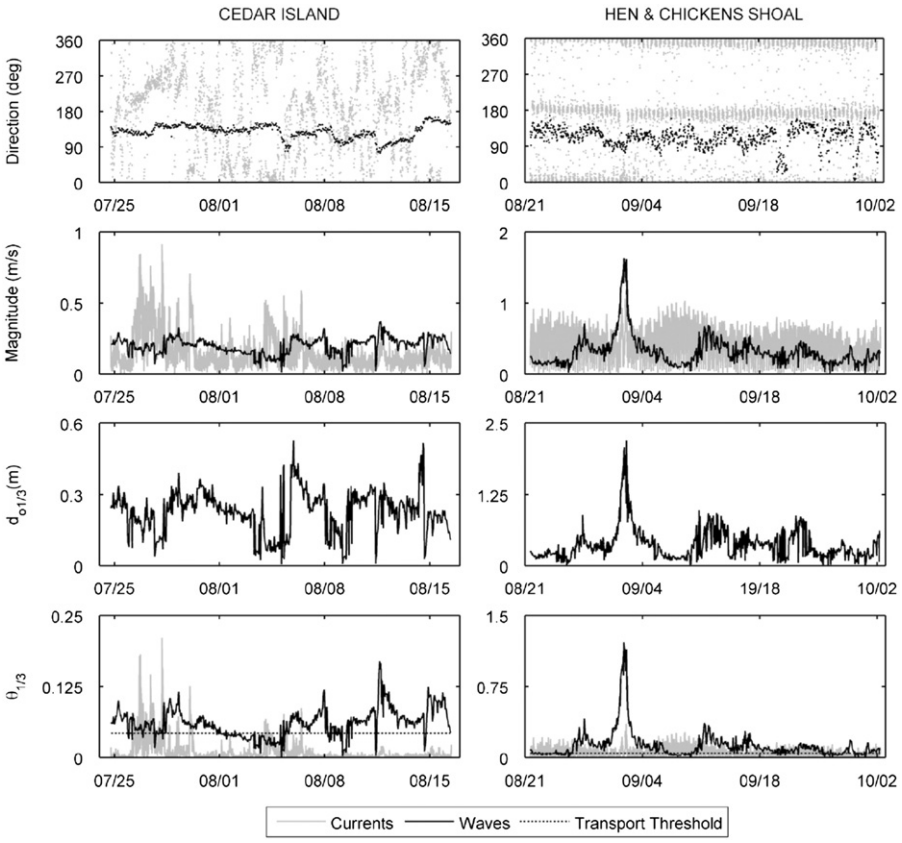

Fig. 3. Hydrodynamic conditions observed during deployments including wave and current azimuthal heading as well as magnitude. The presented wave direction is the direction waves are propagating from, whereas the current direction is the direction currents are propagating towards in accordance with convention. The significant wave orbital diameter and the significant Shields parameter are presented as well.

then opens the next sonar image in chronological order. By completing this procedure for all collected images, a time series of manually determined bedform orientation and wavelength is created. It is important to note that the orientation data is adjusted to avoid the 180° ambiguity of wave crest orientation as well as wraparound issues that are common when plotting orientation data.

Frequency spectra analysis of the sonar images was undertaken through the application of the two-dimensional fast Fourier transform. The code and processing methodology were modifications of those presented by Voulgaris and Morin (2008). First, an image of the entire sonar domain was imported into Matlab and converted to a raster array. Next the image was sub-divided into eight individual images, which are equally spaced around the position of the sonar transducer (Fig. 1B). These overlapping subsamples are located in the sonar near field where acoustic energy is abundant and the seafloor is best defined. Additionally, the subsample images are located around the sonar transducer so that they represent locations where the acoustic beam is parallel as well as orthogonal to the dominant ripple crest orientation. Locations where the beam is perpendicular to the ripple crest provide the best spectral estimates of orientation, while locations where the beam is parallel to ripple crest provide the poorest estimates of orientation. Next each of the eight sub-divided images were resampled to match the median theoretical spatial resolution of the sonar system (i.e. 2.4 cm^2), in order to minimize the potential for artifacts or aliasing. A two-dimensional FFT is then preformed on each sub-sampled image. The resultant spectral peaks are averaged to generate a single peak representative of the entire domain. A parabolic filter is applied at the origin to remove low frequency noise that arises from areas in the sampled images that lack rhythmic geometry. Then, a Gaussian filter is applied to the domain in order to smooth the spectral peak. The ripple wave number coordinates of the spectral peak are determined following the method of Krogstad (2004), and the coordinates are converted to a wavelength and orientation value with the equations presented in Voulgaris and Morin (2008). These values are collected for all images yielding time series of ripple parameters for comparison with the results of other methodologies. In addition to the derived geometric parameters, a non-dimensional reliability parameter, known as the peak index, was calculated for each image, by dividing the power of the spectral peak by the mean power of the entire domain (Voulgaris and Morin, 2008). Peak index describes the height to width relationship of the spectral peak and is representative of a combination of total signal to noise ratio in the image, ripple definition, and consistency in bedform wavelength and orientation across the domain.

Fingerprint analysis techniques are applied to acoustic images of rippled beds in order to create a more sophisticated and representative parameterization of ripple morphology and to address the shortcomings of both manual and FFT analysis. This methodology is based on the fingerprint enhancement and minutiae identification algorithms presented by Hong et al. (1998), and subsequent modifications incorporated into the fingerprint processing code of Kovesi (2000) and Thai (2003). Preprocessing begins with the importation of a rotary sonar image, which is subsequently cropped to remove marginal data outside the effective sonar range (Fig. 4A). Next, the cropped image is normalized in order to standardize the backscatter intensity across the domain, by adjusting the dynamic range of pixel intensity in order to yield a consistent grayscale mean of zero and variance of one. This process does not change the structure of the

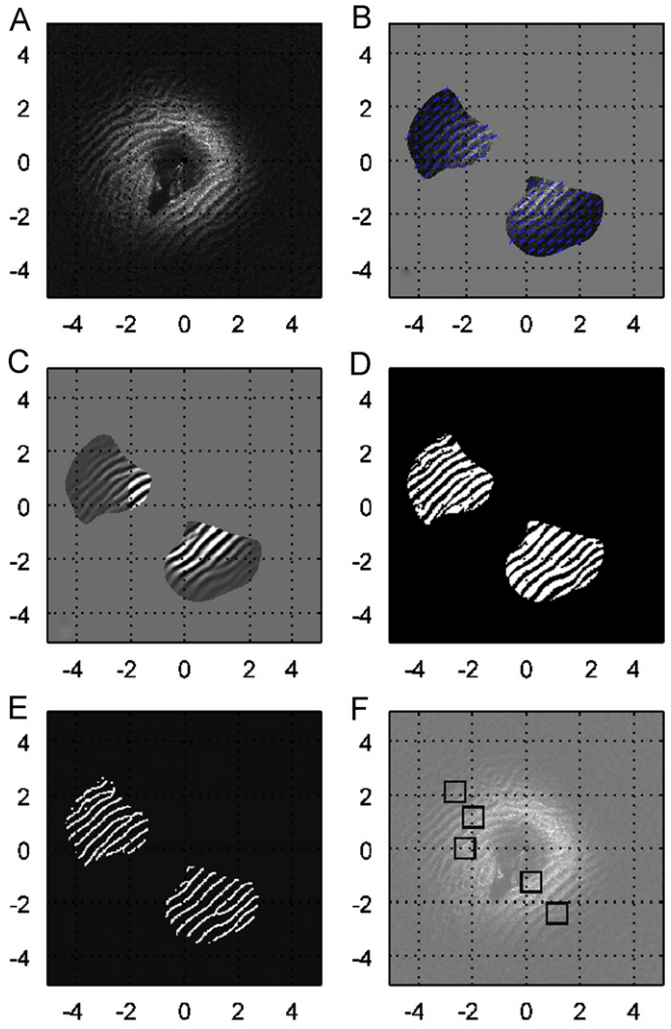

Fig. 4. Rotary sonar image processing. (A) Original image normalized and cropped. (B) Portion of image not meeting ripple threshold removed and ripple orientation calculated (orientation field in blue). (C) Image filtered based on calculated ripple orientation and frequency. (D) Binary image of ripple field. (E) Binary image thinned to line on pixel in width. (F) Locations of ripple defects identified. This image was collected on August 31, 2006, at 16:03:35 GMT during the Hen and Chickens Shoal deployment.

image, but rather standardizes the variance of the images which improves contrast between ridge faces and shadows, as well as facilitating the uniform application of further processing steps.

The local ridge crest orientation is estimated at each pixel by identifying the direction (with 180° ambiguity) orthogonal to the principal axis of variation in Gaussian filtered backscatter gradients within a $W \times W$ sixe block centered on that pixel. The local orientation $\theta(i,j)$is determined with the following equations applied to a $W \times W$ pixel block centered on pixel (i,j):

$$V_x(i,j) = \sum_{u=i-(W/2)}^{i+(W/2)} \sum_{v=j-(W/2)}^{j+(W/2)} 2\partial_x(u,v)\partial_y(u,v) \tag{12}$$

$$V_y(i,j) = \sum_{u=i-(W/2)}^{i+(W/2)} \sum_{v=j-(W/2)}^{j+(W/2)} \partial_x^2(u,v)\partial_y^2(u,v) \tag{13}$$

$$\theta(i,j) = \frac{1}{2} \tan^{-1} \frac{V_y(i,j)}{V_x(i,j)} \tag{14}$$

where $\partial_x(i,j)$ and $\partial_y(i,j)$ are the gradient magnitudes at pixel (i,j) in the x and y directions, respectively (Thai, 2003). For both deployments W was assigned a value of 18 corresponding to a 0.43 m^2 box given the sonar image pixel resolution of 2.4 cm. The least squares estimate of backscatter gradient for the entire box is used to determine the ridge orientation at the central pixel, which always lies orthogonal to the direction of steepest gradient within the box. The resultant orientation values for each pixel in the image are converted to a continuous vector field. It is assumed that the ridge orientation within the domain varies minimally at the spatial scale of the $W \times W$ block, and thus a low-pass Gaussian filter is used to smooth the vector field for the entire domain (Fig. 3B). The frequency of orientation values from each pixel in the domain can then be used to statistically determine orientation variance (standard deviation) and an orientation value (mean or median) representative of the entire image.

The generated continuous vector field is used to determine the "reliability" of orientation data which in turn can be used to generate a mask to exclude data from portions of the image that do not contain ripple information. For each $W \times W$ pixel block, the variability of pixel intensity along the calculated orientation is determined as well as the variability of pixel intensity orthogonal to the derived orientation. The ripple reliability value is calculated as 1.0 – (orientation parallel variability/orientation perpendicular variability). In areas of the domain that are rippled, the along ridge variability is significantly smaller than the across ridge variability yielding a high reliability value. Portions of the domain lacking ripples will have similar variability values parallel and perpendicular to the derived orientation yielding a low reliability value. Once the pixelwise reliability of the sonar image is determined across the domain, a global reliability threshold can be applied and pixels with reliability greater the thresholds are retained as areas of rhythmic morphology while those with variance less than the threshold are excluded from further processing (Fig. 4B).

The ridge wavelength values are determined based upon the continuous vector field of orientation. The image domain is now divided in to $Y \times Y$ pixel blocks, which are large enough to incorporate multiple ripple wavelengths. The local wavelength at each pixel is determined by considering a Gaussian smoothed profile of backscatter values along a line orthogonal to the mean orientation of all pixels in the $Y \times Y$ pixel block centered on that pixel. Local wavelength is at pixel $(i,j)$is evaluated as:

$$F(i,j) = \frac{1}{S(i,j)} \tag{15}$$

where $S(i,j)$ the spatial frequency of localized peaks in the backscatter profile across the Y x Y block (Thai, 2003). This plotted line exhibits a roughly saw-tooth waveform, which is smoothed with a Gaussian low-pass filter to reduce the effects of noise in the image. The ridge spacing is determined by calculating the median number of pixels between consecutive maxima points in the plotted waveform. The block dimensions Y should be based on the native resolution of the image and be significantly larger than the Nyquist frequency for the largest expected ripple wavelength, in order to prevent aliasing effects from being manifest in subsequent processing steps. The widow length in pixels used to determine local maxima points is calculated as the number of times the plotted line crosses its own arithmetic mean divided by the length of the line in pixels. The native resolution of the sonar image can be used to convert the resultant frequency values from pixel units to wavelength distance in meters. Finally, the frequency of wavelength values from each pixel in the domain can then be used to statistically determine wavelength variance (standard deviation) and a wavelength value (mean or median) representative of the entire image.

Next, a filter is applied to the domain in order to preserve the ripple structure and remove noise. The ripple orientation and frequency values derived from the domain are used to create

a two-dimensional Gabor filter. The Gabor filter is composed of a frequency and orientation selective sinusoidal wave. When applied in a blockwise method, this characteristic allows the filter to be tuned to the derived block frequency and orientation, yielding maximal preservation of ripple structure while significantly reducing noise (Fig. 4C). Next, a global binarization threshold is applied to the filtered image, which has a mean intensity of zero. All pixels with intensity values greater than zero are set to a binary value of one, all values less than zero are set to a binary value of zero (Fig. 4D). The foreground portion of the binary image (pixel values=1) is then thinned by removing boundary pixels iteratively, until it is a single pixel in width (Fig. 4E). The resulting image is processed pixelwise in order to identify the location of ripple defect features (Fig. 4F). A 3×3 pixel block centered on each binary pixel with a value of one is considered. If the nine-pixel sum is equal to two, a ripple termination has been identified, and if the nine-pixel sum is equal to 4 a ripple bifurcation has been identified. This processing step yields a new logical binary image in which the location of ripple defect features assigned a value of one and all other pixels are assigned a value of zero. The total number of identified ripple defect features is then normalized by the total area of the sampled portion of the image in order to define a defect density for the image. This normalization can also be applied in a blockwise manner in order to quantity the spatial variability of defect density across a single image. Complete numerical expressions for each of the preceding processing steps are presented in Hong et al. (1998) and Thai (2003).

3. Results and discussion

A comparison of automated methods for deriving ripple wavelength is presented in Fig. 5. The spectral and fingerprint analysis methods were applied to a series of 100 synthetic images of a seafloor with linear ripples with a prescribed wavelength, which varies from 0.1 to 2.5 m. The pixel resolution of the images was 2.4 cm and isotropic noise was added to yield signal to noise ratio of 3. The spectral results have an *R* squared statistic of 0.98 and exhibit better agreement with the prescribed wavelength at lower values. The arithmetic mean of all wavelengths in the image domain determined by the fingerprint method has an *R* squared statistic of 0.99 and displays better agreement with prescribed vales at large wavelength and diminished agreement at wavelengths less than 0.2 m. The mode of all wavelengths in the image domain determined by the fingerprint method has an *R* squared statistic of 0.99 and displays the best agreement with prescribed values, among all methods at large wavelength and the poorest agreement among all methods at wavelengths less than 0.2 m. All three methods display equal skill and a very high capacity to accurately parameterize wavelength for an idealized two-dimensional rippled bed. In order to define the boundaries of applicability for each method with regard to more realistic morphological conditions, synthetic images of the seafloor, with variable prescribed levels of noise and sinuosity, based upon field observations, were processed with the spectral and fingerprint techniques in Fig. 6. In the upper panels of Fig. 6 the spectral and fingerprint analysis methods were applied to a series of 25 synthetic images, with static ripple dimensions and a prescribed signal to noise ratio, which ranges from 0.4 to 2.1. All three methods exhibit good agreement with the prescribed orientation and wavelength at signal to noise rations above one. Below a signal to noise ratio of one, the quality of agreement for all methods degrades, but does so more precipitously for the spectral method, especially in observations of ripple wavelength. In the lower panels of Fig. 6 the spectral and fingerprint analysis methods were applied to a series of 35 synthetic images, with static ripple dimensions and

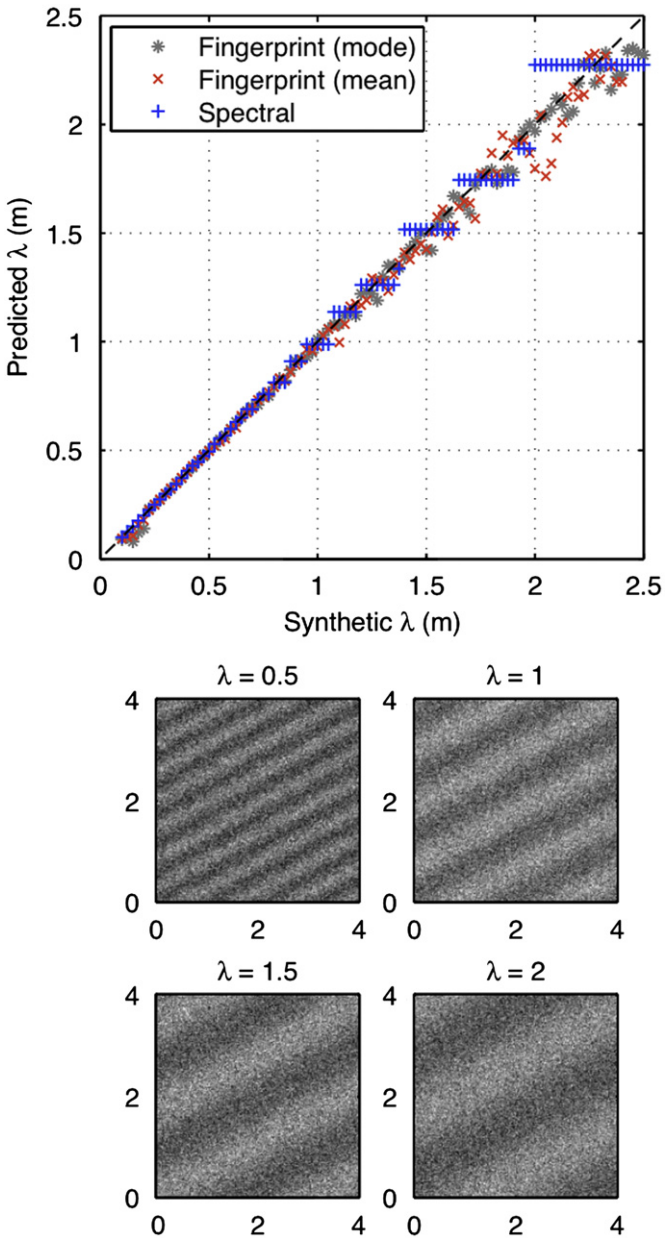

Fig. 5. Scatter plot of a prescribed wavelength versus the fingerprint/spectral determined wavelength for a series of 100 synthetic images with a signal to noise ratio of 3. The dashed line represents equivalence. The *R* squared statistic for the spectral, fingerprint mean, and fingerprint mode data are 0.98 0.99, and 0.99, respectively. Four example synthetic images are presented below the scatter plot.

a ripple planform sinuosity, as defined by the planform amplitude divided by the planform wavelength, which ranges from 0 to 0.2. All methods show agreement with the prescribed orientation and wavelength at values of low planform sinuosity. As ripple sinuosity increases the spectral observations of wavelength and orientation deviate significantly from prescribed values while the two fingerprints remain in much closer agreement. Conditions of high noise and ripple sinuosity are very common in field collected seafloor imagery, and as such, the results presented in Figs. 5 and 6 indicate that the fingerprint method has a higher capacity for parameterizing natural bedform geometry.

A comparison of manual, spectral, and fingerprint methods for deriving ripple orientations and wavelengths for both field deployments is presented in Figs. 7 and 8. For the Cedar Island deployment there is variable agreement between the three

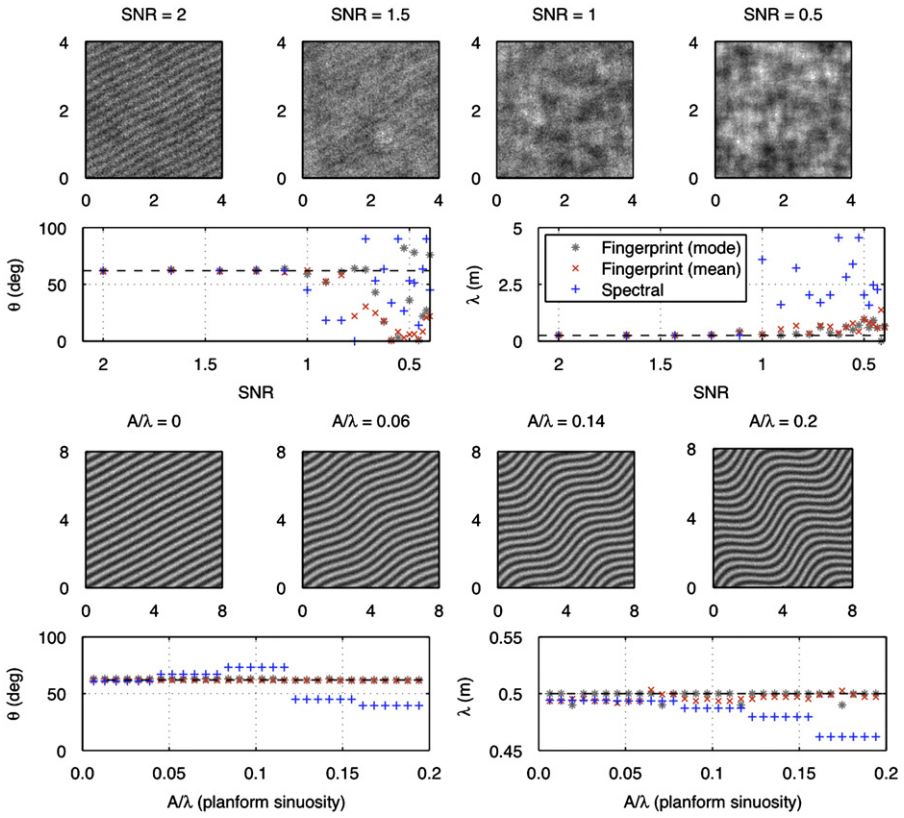

Fig. 6. Plot of determined wavelength and orientation for synthetic images with increasing isotropic noise (top) and increasing planform sinuosity (bottom). Noise is parameterized by a signal to noise ratio and planform ripple sinuosity is parameterized as the planform amplitude divided by the planform wavelength. Four example synthetic images from each trial are presented.

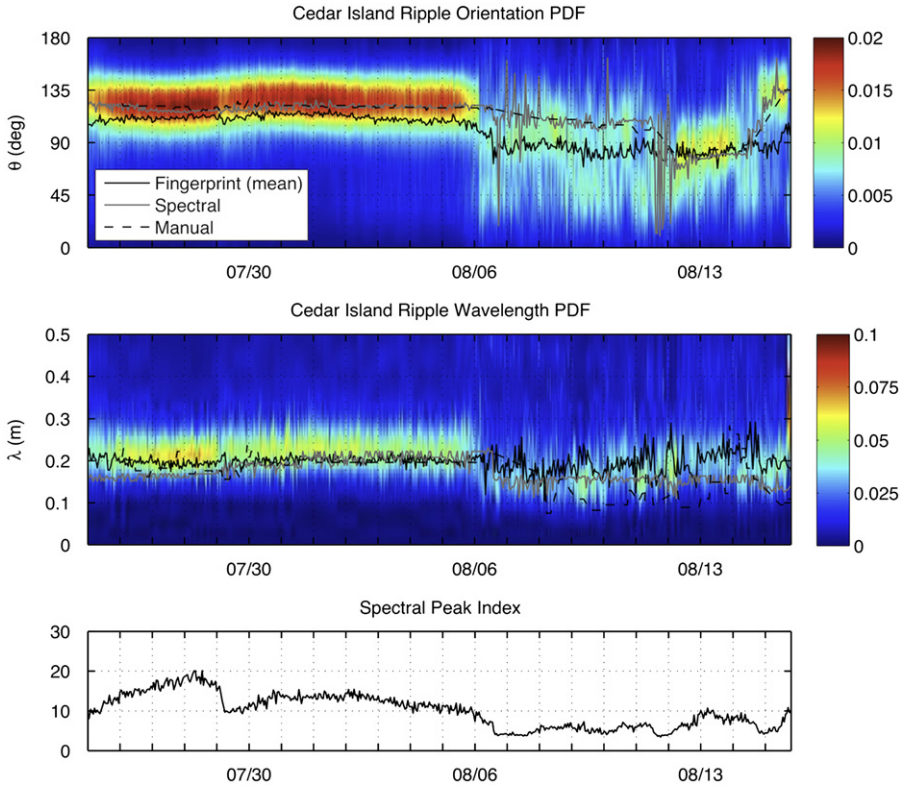

Fig. 7. Comparison of manual, spectral, and fingerprint analysis results for ripple orientation and wavelength at Cedar Island. The colormap represents the probability distribution for orientation and wavelength across the sampled sonar domain as determined by the fingerprint method. The spectral peak index for the deployment based upon the expression of Voulgaris and Morin (2008) is presented at the bottom.

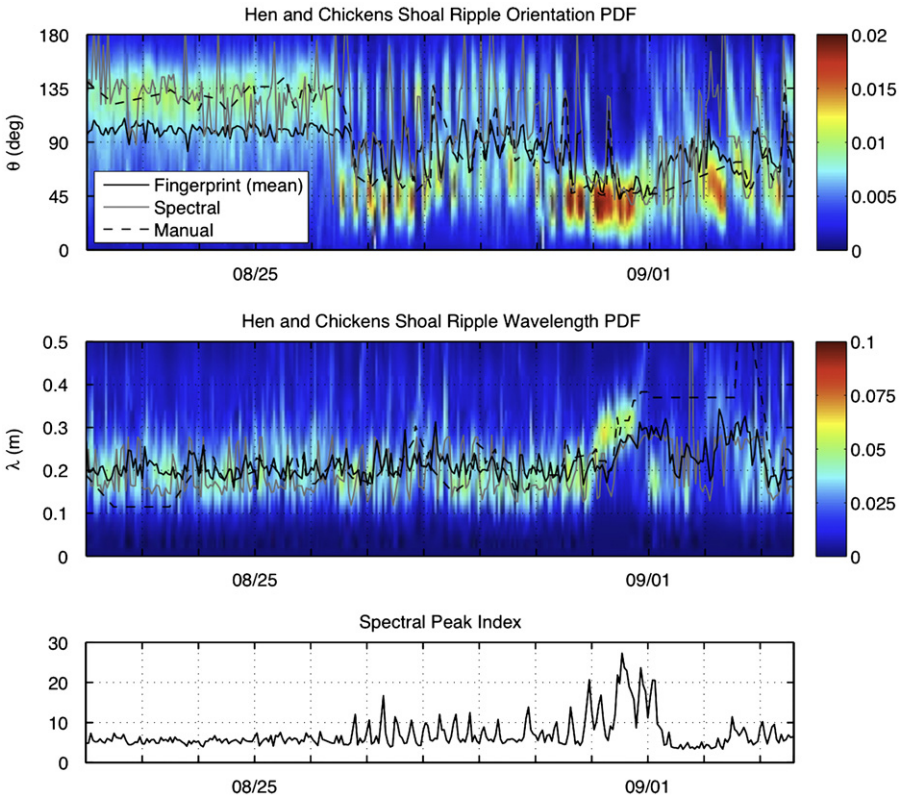

Fig. 8. Comparison of manual, spectral, and fingerprint analysis results for ripple orientation and wavelength at Hen and Chickens Shoal. The shaded area represents the standard deviation of all values extracted from a single image. Colormap represents the probability distribution for orientation and wavelength across the sampled sonar domain as determined by the fingerprint method. The spectral peak index for the deployment based upon the expression of Voulgaris and Morin (2008) is presented at the bottom.

methodologies for both ripple orientation and wavelength. Manual and spectral estimates of ripple orientation agree throughout the deployment and both show a moderate disagreement with the fingerprint mean prior to 8/6 followed by greater disagreement until 8/12 at which point all three methods agree briefly before diverging on 8/14. There is moderate disagreement between all three estimates of ripple wavelength prior to 7/30 at which point all methods agree until 8/7 when they diverge and exhibit increasing disagreement for the duration of the deployment. A sonar image from 7/27 (Fig. 9) indicates that the bed is composed of linear ripples for which the best estimate of orientation is given by the manual method and the mode of orientations derived by the fingerprint method (as indicated by the maximum PDF value in Fig. 7), both of which agree well. The variability in wavelength estimates among all methods is minimal, making a visual confirmation of the most actuate approach impossible. A sonar image from 8/8 (Fig. 9) exhibits significant noise, which may be associated with elevated suspended sediment concentrations, associated with a rapid increase in the current shields parameter during this time. Regardless of the mechanism, the high noise level obscures the bed and suppresses any morphologic signal. This absence of signal in the imagery is likely responsible for the wide range of estimated orientations and may in fact be responsible for the extended period of methodological disagreement from 8/6 to 8/12. Subsequent to this period the bed exhibits linear ripple with a very small wavelength on 18/13 (Fig. 9). During this period of moderately defined bed state, all four methods agree well in their estimates of bed orientation and show significant variability in estimates of bed wavelength. Disagreement among estimates of ripple wavelength may arise from the fact that ripple spacing appears to be very close to the minimum theoretical detectable value (9.6 cm) based upon the resolution of the sonar instrument. This supposition is consistent with results presented in Fig. 5, which indicate variability in wavelength estimates at particularly low values.

For the Hen and Chickens Shoal deployment methodological estimates of ripple wavelength and orientation exhibit poor agreement prior to 8/26 and moderate to good agreement between 8/26 and 9/1. After 9/1 there is a significant degradation in methodological agreement for wavelength and orientation estimates, which persist through the conclusion of the deployment. A sonar image from 8/23 (Fig. 9) during the initial period of significant methodological disagreement exhibits a seafloor with rough but very poorly oriented bed morphology. Orientation estimates of the manual, spectral, and fingerprint mode methods generally agree, whereas the fingerprint mean method is significantly different. The image noise level precludes determination of the best method, but the agreement of three methods suggests they may be more reliable than the outlying fingerprint mean. A sonar image collected on 8/27 (Fig. 9) during a period of poor methodological agreement exhibits well-defined linear ripples. The orientation as determined by the fingerprint mode and manual methods appears to best match the seafloor image. Finally, a seafloor image collected on 8/31 (Fig. 9) during a period of moderate methodological agreement displays very well-defined sinuous ripples. Estimates of ripple orientation yielded by the spectral and fingerprint mode methods appear to best fit the bed orientation imaged by the sonar.

For both deployments, the three analysis methods show better agreement during periods in which sonar images of the bed exhibit more organized bedforms. Observed organized bed states appear, in general, to correlate with periods of consistent magnitude and direction in hydrodynamic forcing or periods of significantly elevated forcing magnitudes both of which are associated with driving the

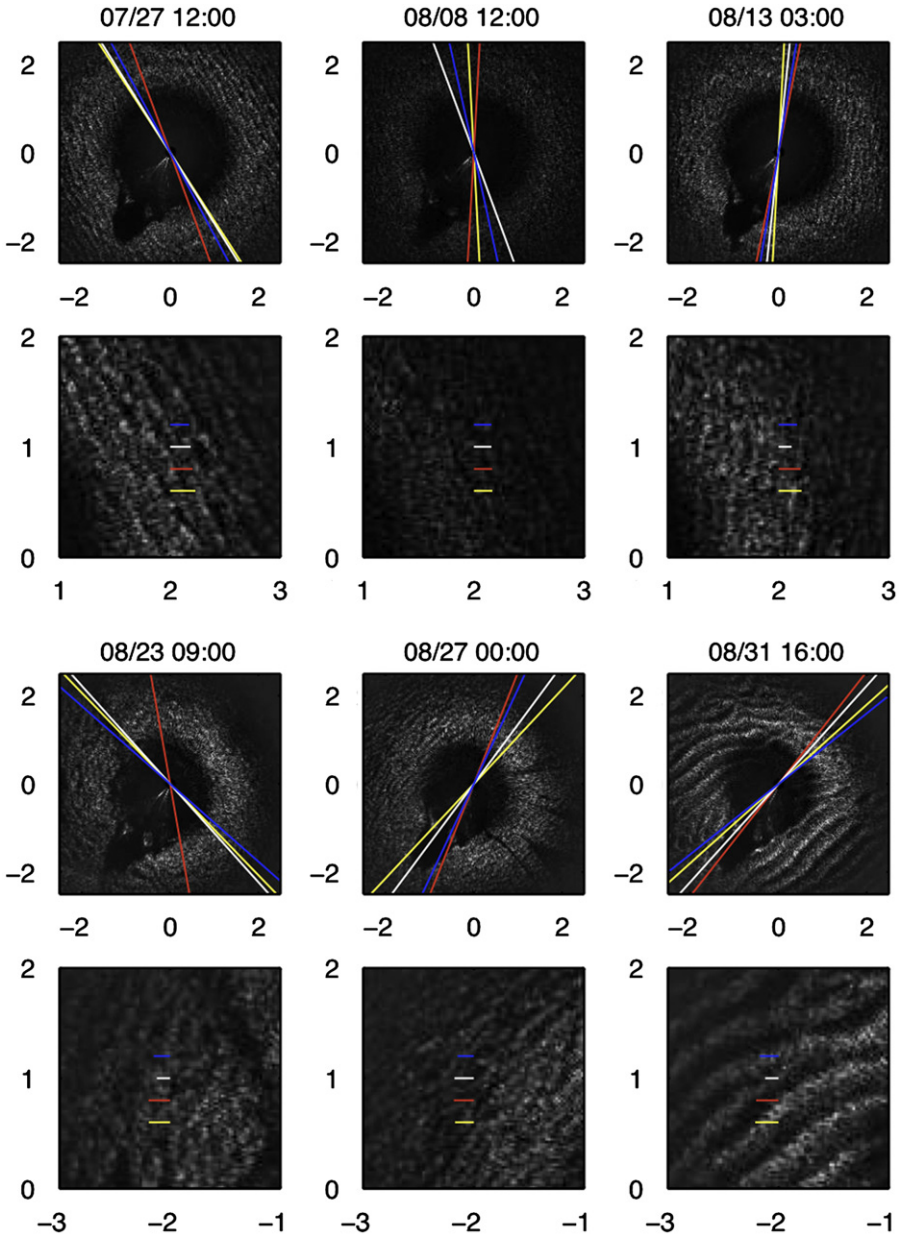

Fig. 9. Raw sonar images from both deployments with the derived ripple orientation and wavelength superimposed. Spectral (blue), fingerprint mean (red), fingerprint mode (yellow), and manual (white). The ripple defect densities/m^2 for each image in chronological order are 10.1, 8.5, 15.9, 9.5, 11.2, and 5.1. (For interpretation of the references to color in this figure legend, the reader is referred to the web version of this article.)

bed towards a state of morphological equilibrium. This relationship is further supported by the peak index as formulated by Voulgaris and Morin (2008), which is a proxy for ripple definition and generally exhibits elevated values during periods of methodological agreement and low values during periods of methodological disagreement (Figs. 7 and 8). Assessment of orientation and wavelength estimates from simulated (Fig. 6) and field images (Fig. 9) indicate that the mode of values across the sampled domain as determined by the fingerprint method is best suited to parameterizing bed morphology especially in conditions of poorly defined or sinuous bed states.

The probability distribution for wavelength and orientation across the "reliable" portions of the sampled domain as determined by the fingerprint method is presented as colormap plots in Figs. 7 and 8 as well. The probability distribution results are unique to the fingerprint method and reveal dynamic spatial variability in the occurrence and deviation of bedform parameters (wavelength and orientation), which appear to have a strong correlation with observed forcing conditions (Shields parameters). Statistical treatment of this data promises to yield not only a single descriptive wavelength and orientation for a seafloor image, but rather a quantitative description of how these parameters vary across the sampled domain. This approach holds great promise for producing improved models of the relationship between hydrodynamic forcing and complex bed morphology such as bimodal orientations related to variable forcing directions or multiple wavelengths as are known to occur with parasitic bedforms. The potential for characterizing morphological parameters probabilistically rather than as a single finite representative value calls for significant analysis, which is beyond the purview of this methodological paper, and will be presented in a forthcoming process based article by the authors.

Fig. 10 presents a time series of ripple defect density as calculated with the fingerprint analysis methodology. During both deployments significant decreases in defect density coincided with rapid increases

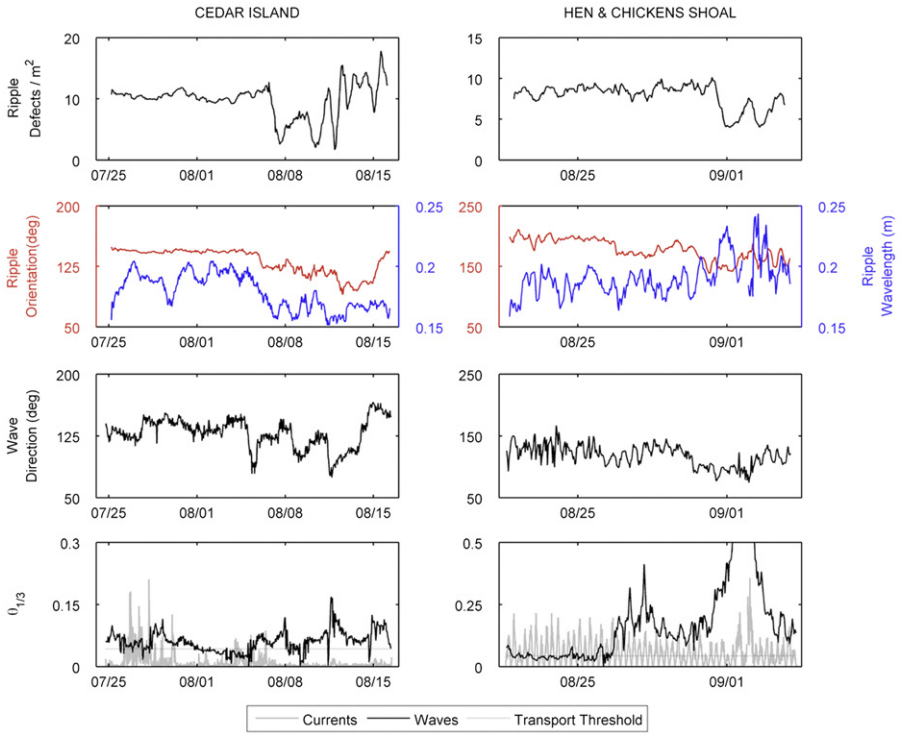

Fig. 10. Ripple defect density plotted relative to observed ripple orientation and wavelength, wave direction, and Shields parameters for waves and currents.

in the Shields parameter likely associated with a storm events. As expected the dominant wave direction responds to these periodic storm events, rotating to the north, and the ripple orientating values follow in turn, though with muted intensity. Downward spikes in defect density correlate well with rapid changes in bedform orientation, which is counter to the hypothesis presented by Maier and Hay (2009) which indicated elevated defect occurrence during times or rapid ripple reorientation. Additionally, sediment transport theory indicates that increases in the Shields parameter value, which coincide with downward deflection in defect density, result in elevated bedform migration rates, supporting the relationship proposed by Werner and Kocurek (1999) . Ripple wavelength does not exhibit a first order correlation with defect density for either deployment. A consideration of the sonar imagery with respect to defect density variability (Fig. 9) suggests that higher defects densities are associated with periods of poor bed definition, where as lower defect densities are associated with periods of greater bed definition. Future efforts will further consider the causality between hydrodynamic forcing parameters and occurrence of bedform defect features.

Although, a majority of this paper has focused on the temporal evolution of ripple parameters within a relatively small domain, the presented fingerprint analysis method is equally useful for making observations of the large-scale spatial variability of ripple morphology. Fig. 9 presets a sub-sample of a side-scan sonar image collected with an autonomous underwater vehicle at the Martha's Vineyard Coastal Observatory (Trembanis et al., 2010). The sonar image is of a sorted bedform feature, which exhibits both mega ripple and anorbital ripple seafloor in close proximity. Because of the native resolution of the image, only the mega ripples are preserved, while the areas with the much smaller anorbital ripples at sub-Nyquist frequency appear featureless. The image is first processed to determine the mega ripple orientation and reliability as in the manner presented in Methods section. Because this operation is pixelwise, the resolution of the calculations matches the native resolution of the image, which is 10 cm^2 in Fig. 9. A threshold is applied to the reliability values of each pixel to isolate the rippled portions of the domain and mask values from non-rippled areas in subsequent results. The three colormap images show the spatial variability of bedform orientation, wavelength, and defect density across the rippled portion of the original image (Fig. 11).

In addition to showing great potential to yield insight into fundamental physical processes occurring at the seabed, fingerprint analysis techniques also produce a number of products particularly valuable to operational defense applications. For example, the ability to rapidly calculate the location and density of bedform defects on side-scan sonar images of the seafloor could be applied to seafloor mine and shipwreck detection (Mayer et al., 2007; Trembanis et al., 2007; McNinch et al., 2006). Partially buried objects such as mines and shipwrecks subjected to scour processes tend to settle downwards until their highest point is approximately level with the surrounding seabed (Trembanis et al., 2007). Scour processes around such an object result in multiple small bedforms in close proximity, which would be manifest on a sonar image as a very dense clustering of ripple defects. A map of the spatial distribution of defect density such as the one presented in Fig. 9 could then be used rapidly target potential mine or shipwreck locations. Ripple orientation calculations and their associated reliability are additional fingerprint analysis products, which could be applied to related defense applications. One of the most challenging environments for identifying seafloor mines are mega-rippled beds because cylindrical ordnance is difficult to visually differentiate from mega ripples in side-scan images. Calculations of ripple reliability allow for differentiation of ripple from non-rippled areas giving a side-scan sonar operator or autonomous vehicle the ability to determine the most important areas to target for survey. Additionally, the calculation of ripple orientation allows an operator or vehicle to plan a survey route orthogonal to the ripple crest so that the shadowing effect of ripples is minimized in the resultant side-scan sonar image (Williams and Coiras, 2010).

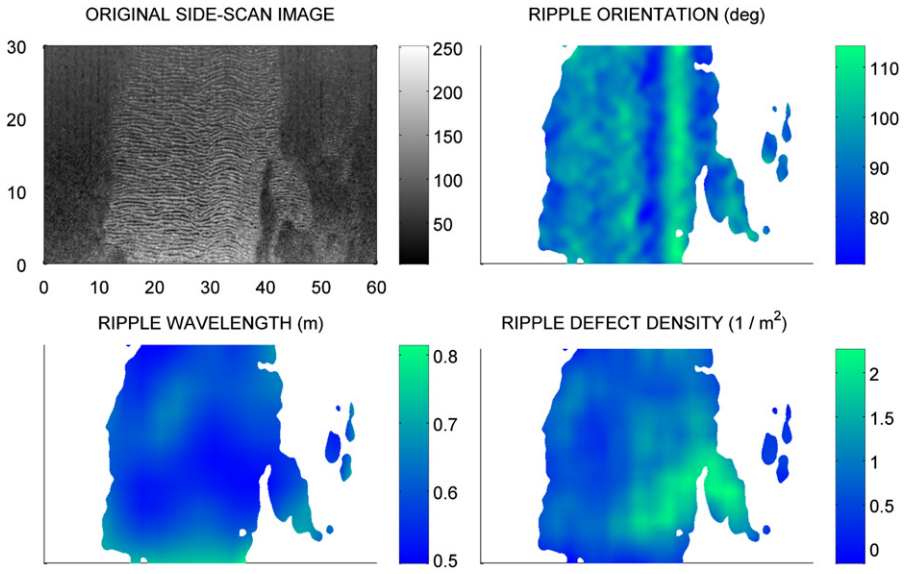

Fig. 11. Side-scan sonar image of seafloor ripples (axes in meters). Parameterization of spatial variability in ripple orientation, wavelength, and defect density. Note automated differentiation of rippled and non-rippled areas in a sorted bedform field.

4. Conclusions

The application of fingerprint analysis methods for ripple parameterization yields a number of improvements over previous methodologies. The new method generates values for ripple orientation and wavelength that are superior to those produced with manual analysis and comparable to those produced with spectral analysis. Additionally, this method generates independent discrete probability distributions for each parameter, and allows for threshold masking of sonar data based upon the degree of seafloor structural orientation, both of which are not possible with the spectral or manual methods. In addition to providing an improved method for deriving widely used bedform parameters, the fingerprint analysis method can evaluate bedform defect density, which is a previously unused parameter that exhibits a strong relationship with observed morphological and hydrodynamic processes. These initial findings indicate the great potential of fingerprint analyses techniques for improved observations of the morphological evolution of the seafloor and suggest that observations of defect density may yield greater insight into bedform morphological processes. Further efforts with regard to this introduced methodology will consider the specific response of beform geometry (including ripple height) and defect density values to wide variety of forcing parameters and seek to establish a quantitative relationship between hydrodynamic flow, bed morphology, and defect behavior.

Acknowledgments

The authors would like to acknowledge the support of Nortek USA incorporated who generously provided the AWAC profiler system for these experiments through their competitive student equipment grant program. We would also like to thank Val Schmidt, Peter Traykovski, and George Voulgaris for helpful discussions on sonar data processing and approaches to ripple geometry estimation. Finally we wish to thank captains Arthur Sundberg, P.G. Ross, Sean Fate, and the crews of the R/V Donna M., R/V Captain White, and R/V Scallop, for their support of field operations and data collection.

References

Cheel, R.A., Hay, A.E., 2008. Cross-ripple patterns and wave directional spectra. J. Geophys. Res. -Oceans. 113, C10009.

Davies, A.G., Villaret, C., 2002. Prediction of sand transport rates by waves and currents in the coastal zone. Cont. Shelf Res. 22, 2725–2737.

Davies, A.G., Thorne, P.D., 2008. Advances in the study of moving sediments and evolving seabeds. Surv. Geophys. 29, 1–36.

Doucette, J.S., 2002. Geometry and grain-size sorting of ripples on low-energy sandy beaches: field observations and model predictions. Sedimentology 49, 483–503.

Englert, C.M., 2010. Development of spectral analyses for rotary sonar images and comparison to predictive ripple models. Eos. Trans. AGU 91 (26) Ocean Sciences Meeting Supplement, Abstract ED25B-13.

Grant, W.D., Madsen, O.S., 1982. Movable bed roughness in unsteady oscillatory flow. J. Geophys. Res.-Oceans. Atmos. 87, 469–481.

Hay, A.E., Mudge, T., 2005. Principal bed states during SandyDuck97: occurrence, spectral anisotropy, and the bed state storm cycle. J. Geophys. Res. –Oceans. 110, C03013.

Hay, A.E., Wilson, D.J., 1994. Rotary sidescan images of nearshore bedform evolution during a storm. Mar. Geol. 119, 57–65.

Hay, A.E., 2008. Near-bed turbulence and relict waveformed sand ripples: observations from the inner shelf. J. Geophys. Res. –Oceans. 113, C04040.

Hong, L., Wan, Y., Jain, A., 1998. Fingerprint image enhancement: algorithm and performance evaluation. IEEE Trans. Pattern Anal. 20, 777–789.

Huntley, D.A., Coco, G., Bryan, K.R., Murray, A.B., 2008. Influence of "defects" on sorted bedform dynamics. Geophys. Res. Lett. 35, L02601.

Irish, J.D., Lynch, J.F., Traykovski, P.A., Newhall, A.E., Prada, K., Hay, A.E., 1999. A self-contained sector-scanning sonar for bottom roughness observations as part of sediment transport studies. J. Atmos. Ocean. Technol. 16, 1830–1841.

Kocurek, G., Ewing, R.C., Mohrig, D., 2010. How do bedform patterns arise? New views on the role of bedform interactions within a set of boundary conditions. Earth Surf. Process. Landforms 35, 51–63.

Kovesi, P.D., 2000. MATLAB and Octave Functions for Computer Vision and Image Processing. School of Earth and Environment, The University of Western Australia. 〈http://www.csse.uwa.edu.au/~pk/research/matlabfns/〉, accessed, March 2008.

Krogstad, H.E., 2004. How to use the MATLAB FFT2-routines. Unpublished Report, 〈http://www.mathworks.com/matlabcentral/fileexchange/11639-how-to-use-fft2〉, accesed, March 2008.

Li, M.Z., Wright, L.D., Amos, C.L., 1996. Predicting ripple roughness and sand resuspension under combined flows in a shoreface environment. Mar. Geol. 130, 139–161.

Li, M.Z., Amos, C.L., 1998. Predicting ripple geometry and bed roughness under combined waves and currents in a continental shelf environemnt. Cont. Shelf Res. 18, 941–970.

Maier, I., Hay, A.E., 2009. Occurrence and orientation of anorbital ripples in nearshore sands. J. Geophys. Res. -Earth Surf. 114, F04022.

Mayer, L.A., Raymond, R., Glang, G., Richardson, M.D., Traykovski, P., Trembanis, A.C., 2007. High-resolution mapping of mines and ripples at the Martha's vineyard coastal observatory. IEEE J. Ocean. Eng. 32, 133–149.

McNinch, J.E., Wells, J.T., Trembanis, A.C., 2006. Predicting the fate of artefacts in energetic, shallow marine environments: an approach to site management. Int. J. Naut. Archaeol. 35, 290–309.

Mogridge, G.R., Davies, M.H., Willis, D.H., 1994. Geometry prediction for wave-generated bedforms. Coast. Eng. 22, 255–286.

Nielsen, P., 1981. Dynamics and geometry of wave-generated ripples. J. Geophys. Res.-Oceans. Atmos. 86, 6467–6472.

Nielsen, P., 1992. Coastal Bottom Boundary Layers and Sediment Transport. World Scientific, Singapore.
Rubin, D.M., Mcculloch, D.S., Hill, H.R., 1983. Sea-Floor-Mounted Rotating Side-Scan Sonar for Making Time-Lapse Sonographs. Cont. Shelf Res. 1, 295–301.
Skarke, A., Trembanis, A., 2008. Micromorphodynamic evolution of bedforms on a transgressive barrier shoreface and cape-associated shoal; Eos Transactions. American Geophysical Union, Ocean Sciences Meeting Supplement., Abstract 165-1248.
Soulsby, R.L., 1997. Dynamics of Marine Sands. Telford, London.
Soulsby, R.L., Whitehouse, R.J.S., 2005. Prediction of ripple properties in shelf seas. Mark 1 predictor, Report TR150. HR Wallingford Ltd. UK for the ONR Ripples DRI Program, 〈http://books.hrwallingford.co.uk/acatalog/free_downloads/TR150.pdf〉.
Swart, D.H., 1974. Offshore Sediment Transport and Equilibrium Beach Profiles. Delft Hydraulics Laboratory, Delft.
Tang, D., Williams, K.L., Thorsos, E.I., 2009. Utilizing High-Frequency Acoustic Backscatter to Estimate Bottom Sand Ripple Parameters. IEEE J. Ocean. Eng. 34, 431–443.
Thai, R., 2003. Fingerprint image enhancement and minutiae extraction. Thesis, University of Western Australia, Crawley.
Thorne, P.D., Hanes, D.M., 2002. A review of acoustic measurement of small-scale sediment processes. Cont. Shelf Res. 22, 603–632.
Traykovski, P., Hay, A.E., Irish, J.D., Lynch, J.F., 1999. Geometry, migration, and evolution of wave orbital ripples at LEO-15. J. Geophys. Res. -Oceans 104, 1505–1524.
Traykovski, P., 2007. Observations of wave orbital scale ripples and a none-quilibrium time-dependent model. J. Geophys. Res 112, C06026.
Trembanis, A.C., Friedrichs, C.T., Richardson, M.D., Traykovski, P., Howd, P.A., Elmore, P.A., Wever, T.F., 2007. Predicting seabed burial of cylinders by wave-induced scour: application to the sandy inner shelf off Florida and Massachusetts. IEEE J. Ocean. Eng. 32, 167–183.
Trembanis, A.C., Skarke, A., Raineault, N., Schmidt, V., Mayer, L., 2010. Detailed variability of ripple geometry within a bedform feature. Geol. Soc. Am. Abstr. Prog. 42, 60.
Voulgaris, G.; Morin, J.P., 2008. A Long-Term Real Time Sea Bed Morphology Evolution System in the South Atlantic Bight, Current Measurement Technology, 2008. CMTC 2008. IEEE/OES 9th Working Conference on, pp.71–79, 17–19 March 2008 doi:10.1109/CCM.2008.4480847.
Werner, B.T., Kocurek, G., 1999. Bedform spacing from defect dynamics. Geology 27, 727–730.
Wiberg, P.L., Harris, C.K., 1994. Ripple geometry in wave-dominated environments. J. Geophys. Res. –Oceans. 99, 775–789.
Williams, D.P., Coiras, E., 2010. On sand ripple detection in synthetic aperture sonar imagery. In: Proceedings of the IEEE International Conference on Acoustics Speech and Signal Processing, March 14–19, 2010, Dallas, TX.
Wright, L.D., 1995. Morphodynamics of Inner Continental Shelves. CRC, Boca Raton.